



PCCP

Computational design of CO-tolerant Pt₃M anode electrocatalysts for proton-exchange membrane fuel cells

Journal:	<i>Physical Chemistry Chemical Physics</i>
Manuscript ID	CP-ART-11-2018-007086.R2
Article Type:	Paper
Date Submitted by the Author:	07-Jan-2019
Complete List of Authors:	Liu, Yulu; The University of Texas at Austin, Chemistry; Sichuan University, Duan, Zhiyao; The University of Texas at Austin, Chemistry Henkelman, Graeme; The University of Texas at Austin, Chemistry

SCHOLARONE™
Manuscripts

Computational design of CO-tolerant Pt₃M anode electrocatalysts for proton-exchange membrane fuel cells

Yulu Liu,^{†,¶} Zhiyao Duan,^{‡,¶} and Graeme Henkelman^{*,‡}

[†]*College of Architecture and Environment, Sichuan University, 24 South Section 1 Ring Road No. 1, Chengdu, Sichuan Province 610065, P. R. China*

[‡]*Department of Chemistry and the Institute for Computational Engineering and Sciences, The University of Texas at Austin, 105 E. 24th Street, Stop A5300, Austin, TX 78712-0165, USA*

[¶]*Contributed equally to this work*

E-mail: henkelman@utexas.edu

Abstract

CO is a common contaminant in hydrogen fuel produced via steam reforming. Development of a CO-tolerant Pt-based anode for the proton-exchange membrane fuel cells (PEMFC) is of great interest to avoid catalyst deactivation caused by strong CO adsorption on Pt. Pt-Ru, Pt-Mo, and Pt₃Sn are three known Pt-based bimetallic CO-tolerant anode materials. The enhanced CO-tolerance of these alloys has been generally attributed to a bifunctional effect enabling oxidative CO removal at low applied potential and a ligand effect between the two metals which weakens CO bonding and reduces CO surface coverage. In this study, we use density functional theory to calculate surface adsorption states under reaction conditions for Pt-based alloys. Our calculations provide a molecular-level understanding of the enhanced CO-tolerance of

Pt alloys induced by the second metal. We find that Mo and Sn dopants promote CO-tolerance by reducing CO surface coverage and enabling CO oxidative removal at low applied potential. On the other hand, Ru is not able to promote CO electro-oxidation at the low applied potential of the operating conditions of a PEMFC anode. The CO-tolerance induced by Ru is attributed to the reduction of CO coverage on Pt sites. Based on these mechanisms, we carried out a computational screening of Pt₃M electrocatalysts for CO-tolerant PEMFC anodes. A number of promising candidates have been identified for experimental examination.

Keywords

CO electro-oxidation, platinum alloys, CO-tolerant anodes, bifunctional effect, ligand effect, proton-exchange membrane fuel cell

Introduction

Pt is the best monometallic anode material for proton-exchange membrane fuel cells (PEMFCs). However, Pt can be easily poisoned by trace amounts of CO impurity in the hydrogen fuel. The CO impurity cannot be completely avoided during hydrogen fuel production from natural gas since the water-gas shift reaction is only mildly exothermic and so there will be some equilibrium concentration of reactant CO with the H₂ and CO₂ products. Thus, the development of CO-tolerant anode materials is particularly important. It has been demonstrated that alloying Pt with a second metal is a working strategy to make Pt anodes CO-tolerant. Among these Pt alloys, Pt-Ru,¹⁻⁵ Pt-Mo,⁶⁻⁸ and Pt₃Sn⁹⁻¹³ are the best-known.

The effects introduced by the second metal are proposed to be two-fold: the bifunctional effect and the ligand effect. In the bifunctional mechanism, water is exclusively oxidized on the alloying metal to form adsorbed OH, which then reacts with adsorbed CO on the Pt sites. Consequently, facile oxidative removal of adsorbed CO reduces the steady-state coverage of

adsorbed CO, freeing Pt sites for hydrogen oxidation. The ligand effect, on the other hand, attributes the CO-tolerance to a change in the electronic structure of the Pt, induced by the second metal such that the CO adsorption strength is reduced and so lowers the CO coverage. These two effects are generally operating simultaneously and separating them has been difficult experimentally. In addition, attributing the promoting effect of the alloying metal to one or two factors may oversimplify the actual mechanism. While both Pt-Mo and Pt₃Sn are thought to follow the bifunctional mechanism for CO electro-oxidation,¹⁴ their reaction orders with respect to CO partial pressure are qualitatively different. Pt-Mo and Pt-Ru have negative reaction orders, whereas the reaction order for Pt₃Sn is positive.^{6,12}

In this study, we use first-principles thermodynamics to determine the equilibrium surface adsorption states of Pt₃M catalysts under reaction conditions to provide an understanding of their CO-tolerance. First, we determine the mechanisms of CO electro-oxidation and CO tolerance on Pt, Pt₃Mo, Pt₃Ru, and Pt₃Sn surfaces. Second, we carry out a computational screening of Pt₃M electrocatalysts (M = *d*-block and *p*-block metals) from which a number of new promising CO-tolerant Pt-based electrocatalysts have been identified.

Computational methods

Spin-polarized density functional theory (DFT) calculations with a plane-wave basis set were performed using the Vienna *Ab initio* Simulation Package.^{15–17} The generalized gradient approximation with the revised Perdew-Burke-Ernzerhof (RPBE) functional¹⁸ was used to calculate electronic exchange and correlation energies. The core electrons were described with the projector augmented wave method.¹⁹ In all calculations, the energy cutoff of the plane wave basis set was 400 eV. The Brillouin zone was sampled using the Monkhorst-Pack scheme²⁰ with a $4 \times 4 \times 1$ *k*-point mesh for the $p(2 \times 2)$ Pt(111) surface slab. We have also employed a $(\sqrt{3} \times \sqrt{3})$ Pt(111) surface slab, whose Brillouin zone was sampled by a $6 \times 6 \times 1$ *k*-point mesh. Optimized structures were obtained by minimizing the forces on

each ion until they fell below 0.01 eV/Å. Structures of clean and adsorbate-covered Pt(111) and Pt₃M(111) surfaces were modeled within the supercell approach using slabs consisting of four metal layers. The positions of the atoms in the bottom two-layer were fixed in bulk positions. A 20 Å vacuum layer was used to separate periodic images of the slabs. The lattice constant of Pt was computed to be 3.99 Å. Convergence of binding energies with respect to k-point sampling, plane wave energy cutoff, and slab thickness have been tested in Ref. 21. For Pt₃M (111) models, one of the surface Pt atoms is replaced by a different metal element to create a Pt₃M surface alloy.

Based on the calculated energies, we construct the surface phase diagram to show the favorable surface states under reaction conditions of CO electro-oxidation. The method is based on the computational hydrogen electrode method^{22,23} and ab-initio thermodynamics.²⁴ Stable surface phases under reaction conditions are found by calculating their specific free energy of formation based upon various proposed atomic structures. The surface phases with the lowest free energy of formation are present on the surface phase diagram. The specific free energy of formation is calculated as:

$$\Delta\gamma = \frac{1}{A_S} \left(G_{\text{ads/slab}} - G_{\text{slab}} - \sum_i n_i \mu_i \right). \quad (1)$$

In the above equation, $G_{\text{ads/slab}}$ and G_{slab} are the Gibbs free energies of the adsorbate-covered and clean surface, n_i is the number of adsorbed atoms of type i per surface area A_S , and μ is the chemical potential of the adsorbates in their corresponding reservoir. In this study, we are concerned with the chemical potentials of CO, water, and oxygenated species generated through electrochemical water oxidation. The chemical potential of CO is determined from thermodynamic equilibrium with a gas-phase reservoir. Thus, the CO chemical potential depends on temperature and pressure according to

$$\mu_{\text{CO}}(T, p_{\text{CO}}) = E_{\text{CO}}^{\text{tot}} + \tilde{\mu}_{\text{CO}}(T, p^0) + k_{\text{B}}T \ln \frac{p_{\text{CO}}}{p^0}, \quad (2)$$

where p^0 is the standard pressure, and $\tilde{\mu}_{\text{CO}}(T, p^0)$ is the chemical potential at p^0 , which is obtained from thermodynamical tables.²⁵ The temperature- and pressure-dependent terms in Equation 2 are further combined into a single term, so that the chemical potential of CO can be simplified to $\mu_{\text{CO}} = E_{\text{CO}}^{\text{tot}} + \Delta\mu_{\text{CO}}(T, p_{\text{CO}})$. The chemical potential of water in liquid phase at standard conditions is calculated as the chemical potential of a gas-phase water molecule at 0.035 bar because at this pressure, a gas-phase water molecule is in equilibrium with liquid water.²² Hence, $\mu_{\text{H}_2\text{O}} = E_{\text{H}_2\text{O}}^{\text{tot}} + \Delta\mu_{\text{H}_2\text{O}}(T, 0.035 \text{ bar})$. The electrochemical potentials of O and OH are calculated according to electrochemical reactions:



The chemical potential of the solvated proton and electron pair ($\text{H}^+ + \text{e}^-$) is calculated as $\frac{1}{2}\mu_{\text{H}_2} + eU_{\text{SHE}} - k_{\text{B}}T \ln(10)\text{pH}$ assuming equilibrium at the standard hydrogen electrode, where $\mu_{\text{H}_2} = E_{\text{H}_2}^{\text{tot}} + \Delta\mu_{\text{H}_2}(T, 1 \text{ bar})$. Then, the electrochemical potentials of O and OH are calculated using the above electrochemical reactions as $\mu_{\text{OH}} = \mu_{\text{H}_2\text{O}} - (\frac{1}{2}\mu_{\text{H}_2} + eU_{\text{SHE}} - k_{\text{B}}T \ln(10)\text{pH})$ and $\mu_{\text{O}} = \mu_{\text{H}_2\text{O}} - (\mu_{\text{H}_2} + 2eU_{\text{SHE}} - 2k_{\text{B}}T \ln(10)\text{pH})$. Finally, it is common practice to replace the free energies of solid surfaces, with or without adsorbates, with total energies due to the small enthalpic and entropic contributions as compared to the gas-phase or liquid phase molecules.²⁴ Hence the surface free energy of formation is reformulated as:

$$\Delta\gamma = \frac{1}{A_{\text{S}}} \left(\Delta E_{\text{ads}} - \sum_i n_i \Delta\mu_i(T, p, U) \right), \quad (5)$$

where ΔE_{ads} are the adsorption energies calculated using total energies. Room temperature of $T = 298.15 \text{ K}$ is assumed throughout this study. Dispersion, vibrational entropy, and zero-point corrections are not included in our calculations since previous studies have shown that they have a negligible contribution to relative binding energies of similar adsorbates.²⁶ Note

that in this particular formulation the dependence of the free energy of adsorption on entropic contributions enters entirely through the corresponding dependence of the electrochemical potentials of the species in the reservoir based upon the temperature, pressure, and electrode potential.

To construct the surface phase diagram, various surface adsorption states were calculated including CO, OH, and O adsorption, as well as CO/OH and CO/O co-adsorption states. Many different adsorption sites and surface coverages were considered; the minimum number of such surface states that were considered to construct each surface phase diagram was 40. For pure the Pt(111) surface, OH/H₂O co-adsorption states and the surface PtO₂ oxide were also considered. The binding energies that were used to generate the surface phase diagrams in this paper have been included in the supporting information.

Results and discussions

Surface phase diagram of Pt(111)

The calculated surface phase diagram for Pt(111) as a function of $\Delta\mu_{\text{CO}}$ and applied potential is shown in Figure 1. There are three stable CO adsorption phases depending on the partial pressure of the CO gas. We assume there is a 10 ppm concentration of CO in H₂ at 1 atm. At $p_{\text{CO}} = 10^{-5}$ atm, the CO coverage on Pt(111) is 0.75 monolayer (ML) with the structure of $p(2 \times 2)\text{-3CO}^{\text{fcc,hcp,top}}$. This predicted structure is consistent with experimental findings.^{27,28} When CO is absent, O generated from water oxidation would start to adsorb on the Pt(111) surface when the applied potential is 0.75 V/RHE. The coverage of the adsorbed O is 0.25 ML. Upon increasing the applied potential to 1.1 V/RHE, a ML of $\alpha\text{-PtO}_2$ develops on the Pt(111) surface. The $\alpha\text{-PtO}_2/\text{Pt}(111)$ surface oxide structure has been observed previously in a low energy electron diffraction study, when the Pt surface was annealed in an oxygen environment.²⁹ At $p_{\text{CO}} = 10^{-5}$ atm, the adsorbed CO is depleted from the surface by the formation of the surface oxide at $U = 1.1$ V/RHE. We would expect that

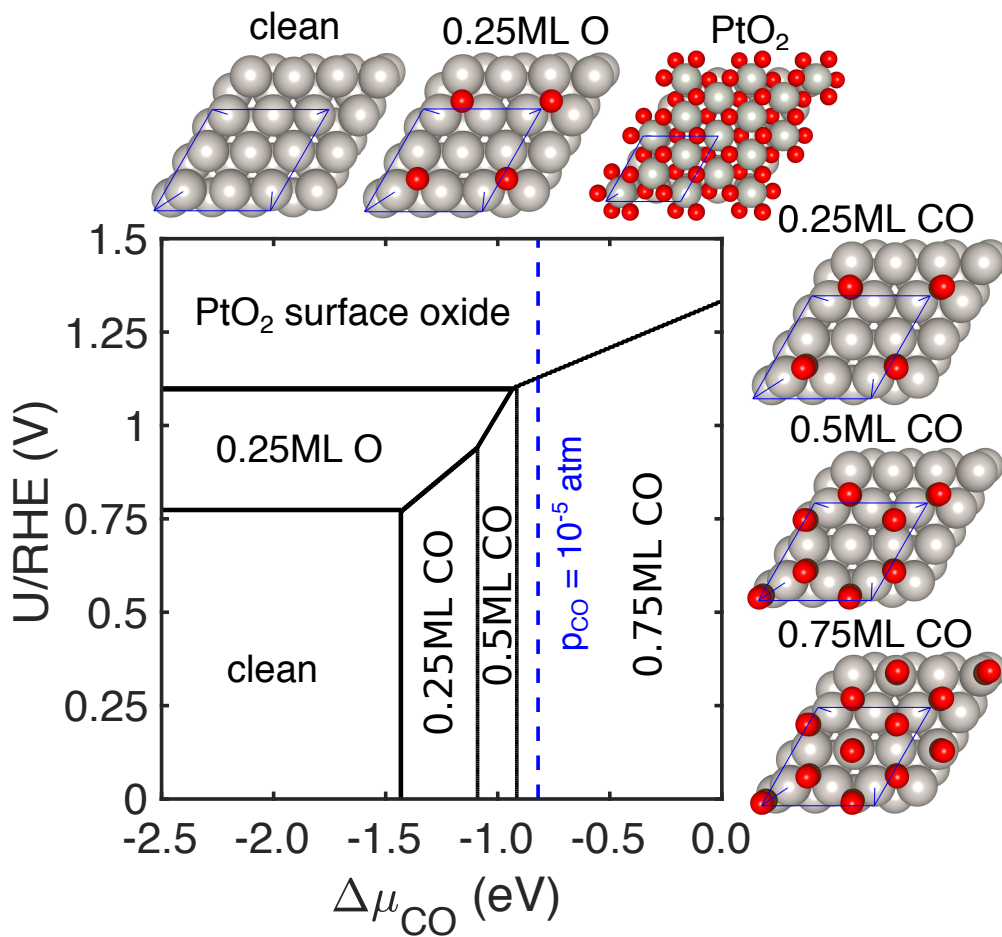


Figure 1: Surface phase diagram for Pt(111). The atomic structures for stable surface states are shown next to the surface phase diagram. The blue dashed line indicates the chemical potential of CO gas corresponding to a partial pressure of 10^{-5} atm at $T = 298.15$ K. Grey, brown, and red balls represent Pt, C, and O elements, respectively.

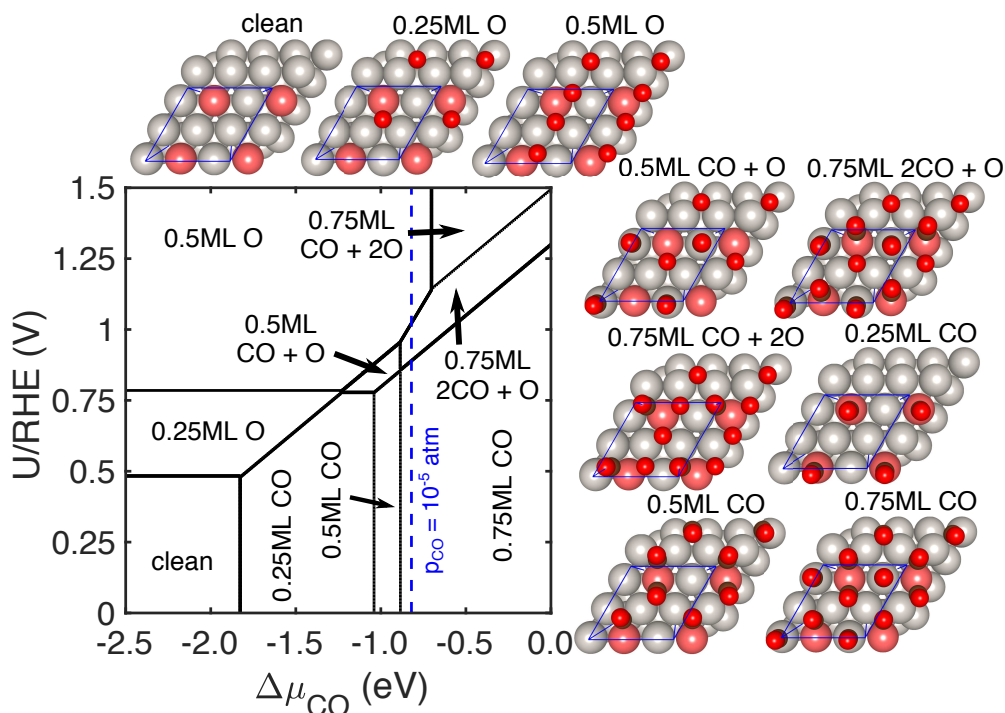


Figure 2: Surface phase diagram for $\text{Pt}_3\text{Ru}(111)$. The atomic structures for stable surface states are shown alongside the surface phase diagram. The blue dashed line indicates the chemical potential of CO gas corresponding to a partial pressure of 10^{-5} atm at $T = 298.15$ K. Grey, pink, brown, and red balls represent Pt, Ru, C, and O elements, respectively. The same pressure, temperature, and coloring of atoms apply to all subsequent figures of phase diagrams.

at the boundary of the surface state transition, the activity of CO electro-oxidation should be high since adsorbed CO should readily react with O atoms in the surface oxide as it starts to form. Below this potential, the Pt(111) surface is poisoned by 0.75 ML of adsorbed CO, which causes a high over-potential for the CO electro-oxidation reaction (1.1 V/RHE vs. the equilibrium potential of -0.1 V/RHE). Likely, the hydrogen oxidation reaction (HOR) is also hindered by the high coverage of CO on the Pt(111) surface if no available Pt sites are available.

Surface phase diagram of Pt₃Ru(111)

The calculated surface phase diagram for Pt₃Ru(111) as a function of $\Delta\mu_{\text{CO}}$ and applied potential is shown in Figure 2. The doped Ru is expected to enhance water activation. Indeed, we see that the adsorbed 0.25 ML O state occurs at 0.5 V/RHE when CO is not present in the environment, which is lowered by 0.25 V as compared to that on the Pt(111) surface. CO adsorption is also much stronger on the Ru site. The 0.25 ML CO adsorption state, in which a CO molecule adsorbs atop a Ru atom, occurs at $\Delta\mu_{\text{CO}} = -1.8$ eV – much lower than that on the Pt(111) surface. In the 0.5 ML CO adsorption state, two CO molecules are both adsorbed on the Ru site. At $p_{\text{CO}} = 10^{-5}$ atm, adsorbed CO molecules cover 0.75 ML of the surface with one more CO atop Pt compared to the 0.5 ML CO adsorption state.

In addition to the pure O and CO adsorption states, there are two mixed CO and O surface states; 0.5 ML CO + O and 0.75 ML 2CO + O show up on the surface phase diagram. At $p_{\text{CO}} = 10^{-5}$ atm, the 0.75 ML CO adsorption state transitions to the 0.75 ML 2CO + O state at 0.9 V/RHE. We expect that the mixed surface state possesses high activity for CO electro-oxidation since CO and the oxidants are thermodynamically available on the surface and will readily react with each other.

Compared to the Pt(111) surface, Ru lowers the over-potential for CO electro-oxidation by 0.2 V due to its stronger interaction with oxygenated species in a manner that can be described as a bifunctional effect. It can be seen that in the 0.5 ML CO + O phase, CO is adsorbed atop Pt and O is adsorbed at the Pt₂Ru 3-fold hollow site. However, the over-potential is still high and unlikely to promote the HOR through oxidative CO removal at the operating potential of PEMFC anodes (0 to 0.4 V/RHE). The enhanced HOR activity could be due to the slight reduction in the coverage of CO. From the surface phase diagram of Pt₃Ru(111), the blue dashed line indicating a $\Delta\mu_{\text{CO}}$ value of $p_{\text{CO}} = 10^{-5}$ atm is closer to the boundary line of the 0.5 ML CO/0.75 ML CO phase, as compared to the case of the Pt(111) surface. This change is partially caused by the ligand effect induced by Ru, making CO adsorption on Pt weaker comparing to pure Pt. Specifically, the adsorption energy of

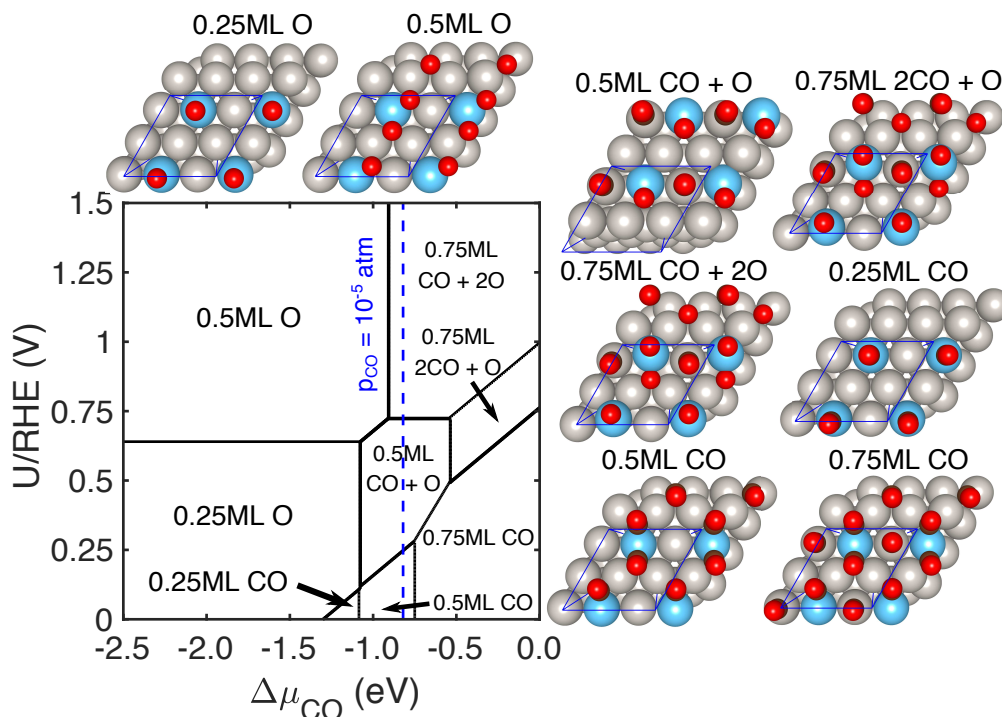


Figure 3: Surface phase diagram for $\text{Pt}_3\text{Mo}(111)$.

CO adsorbed atop Pt is changed from -1.43 eV on the pure Pt surface to -1.31 eV when Ru is present.

Surface phase diagram of $\text{Pt}_3\text{Mo}(111)$

The calculated surface phase diagram for $\text{Pt}_3\text{Mo}(111)$ as a function of $\Delta\mu_{\text{CO}}$ and applied potential is shown in Figure 3. O atoms adsorb strongly on Mo sites. The stable surface state is 0.25 ML O even at $U = 0$ V/RHE. Unlike $\text{Pt}(111)$ and $\text{Pt}_3\text{Ru}(111)$, where the adsorbed O remains at the 3-fold hollow sites, the adsorbed O exclusively resides atop Mo on the $\text{Pt}_3\text{Mo}(111)$ surface. The CO adsorption structures are similar to those discussed in the Pt_3Ru case. However, the Mo induced ligand effect on neighboring Pt atoms leads to weaker CO adsorption on Pt as compared to the Ru alloy. Specifically, the adsorption energy of CO adsorbed atop Pt changes from -1.43 eV on pure Pt to -1.24 eV when Mo is present. As a result, at $p_{\text{CO}} = 10^{-5}$ atm, the equilibrium CO coverage on $\text{Pt}_3\text{Mo}(111)$ is

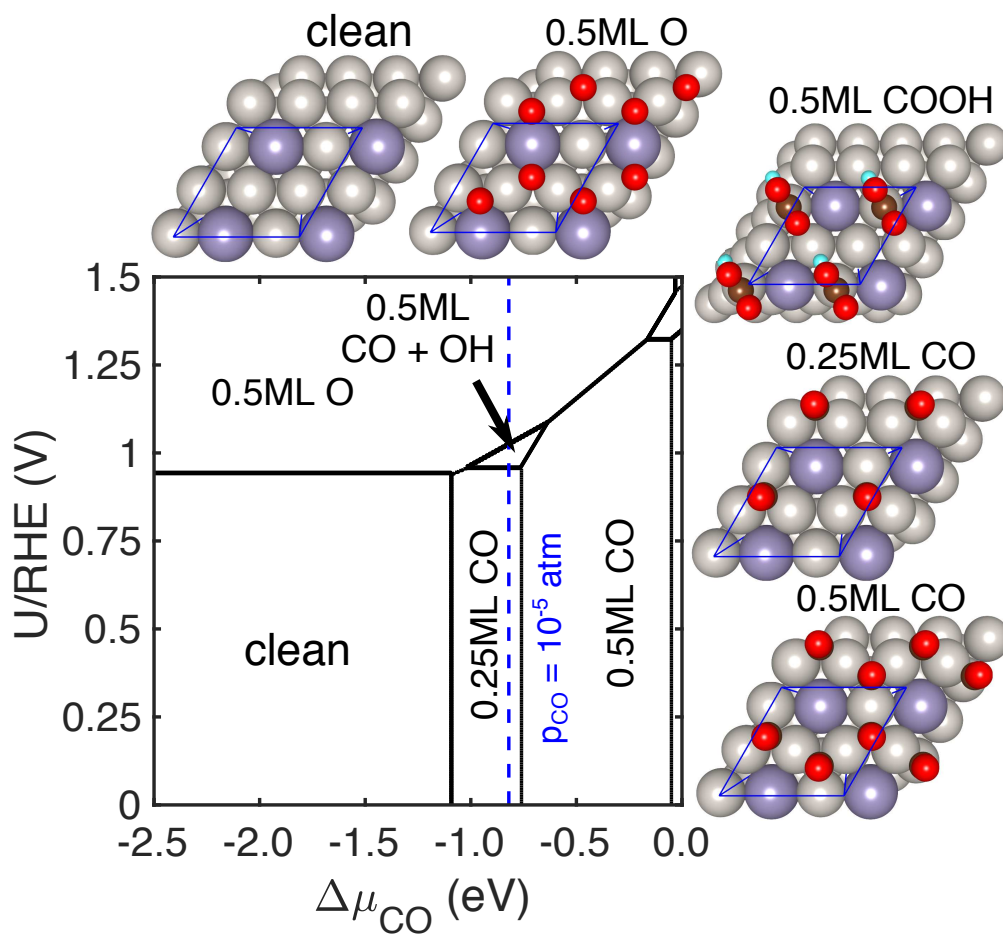
only 0.5 ML, where a Pt site is free of adsorbates. We expect that this Pt site is available for the HOR.

At $p_{\text{CO}} = 10^{-5}$ atm, the mixed 0.5 ML CO + O is present on the surface phase diagram at a potential as low as 0.25 V/RHE. Thus, Mo promotes water activation at low potential creating an active mixed CO and O phase. Also, since O adsorbs atop Mo without binding to Pt atoms, the CO tolerance of Pt₃Mo can be more purely attributed to the bifunctional effect as compared to the previously-discussed Pt₃Ru case. CO electro-oxidation occurs at a potential as low as 0.25 V/RHE, which benefits HOR activity in the presence of CO by rapidly removing adsorbed CO from the surface.

Surface phase diagram of Pt₃Sn(111)

The calculated surface phase diagram for Pt₃Sn (111) as a function of $\Delta\mu_{\text{CO}}$ and applied potential is shown in Figure 4. An obvious effect induced by the Sn dopant is that the CO coverage is dramatically reduced due to the ligand effect of Sn on neighboring Pt atoms. Specifically, the adsorption energy of CO adsorbed atop Pt is reduced from -1.43 eV on pure Pt to -1.09 eV when Sn is present. Combined with the fact that CO cannot adsorb on Sn atoms, at $p_{\text{CO}} = 10^{-5}$ atm, the CO coverage is only 0.25 ML. Unlike Ru and Mo, Sn cannot effectively activate water. The 0.5 ML O adsorption state only presents at potentials above 0.94 V/RHE. These calculations show that the Pt₃Sn(111) surface cannot form an “active phase” in which oxygenated species and adsorbed CO are both present on the surface at low applied potentials. This theoretical prediction is inconsistent with the experimental observation that Pt₃Sn(111) can catalyze CO electro-oxidation at a potential as low as 0.2 V.¹² This inconsistency is resolved by the fact that oxygenated species are formed kinetically at the Sn site, as discussed below.

To further investigate the reaction mechanism of CO electro-oxidation on Pt₃Sn, we plot the potential energy profile for CO oxidation in Figure 5a, along with that of Pt, Pt₃Ru, and Pt₃Mo. We assume that CO adsorbs on Pt and water is activated on Sn to form adsorbed

Figure 4: Surface phase diagram for Pt₃Sn(111).

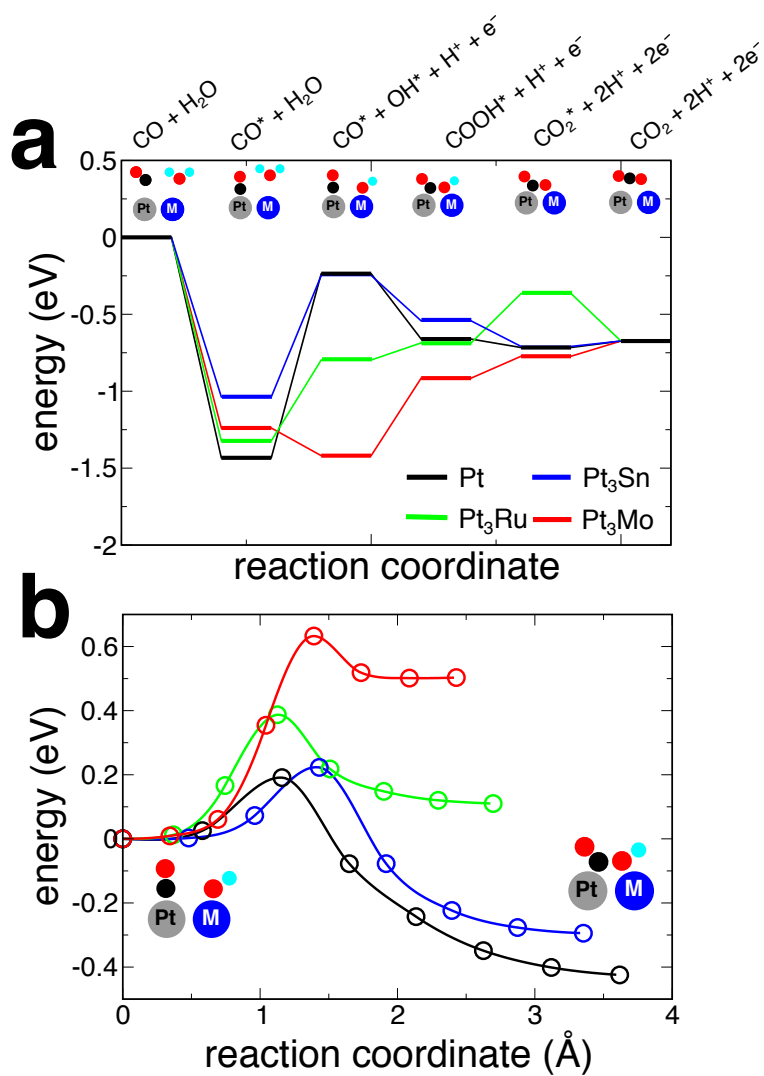


Figure 5: (a) Potential energy surface of CO electro-oxidation reaction on Pt(111), Pt₃Sn(111), Pt₃Ru(111), and Pt₃Mo(111). (b) Energy barriers of CO and OH combination to form COOH on Pt(111), Pt₃Sn(111), Pt₃Ru(111), and Pt₃Mo(111) surfaces.

OH. Then, CO and OH react to form adsorbed COOH, and COOH dehydrogenates to form adsorbed CO₂. Finally, the adsorbed CO₂ desorbs into the gas phase. All potential energy profiles were calculated at $U = 0$ V.

It can be seen that water activation on Sn, which is endothermic by 0.75 eV, is the rate-determining process at $U = 0$ V. The energy increase of this step is reduced by 0.5 eV as compared to the pure Pt surface as shown in Figure 5a. However, at the experimental onset potential for CO electro-oxidation on the Pt₃Sn(111) surface, *i.e.* 0.2 – 0.3 V/RHE, water activation remains an endothermic process by 0.5 eV. That is why oxygenated species are not found at this potential range in the surface phase diagram. However, this energy can be surmounted at operating conditions of a PEMFC ($T = 60^\circ\text{C}$), resulting in a kinetically adsorbed OH atop the Sn site.

Alternatively, water activation could follow the Eley-Rideal mechanism, in which the energy cost of water activation is compensated by C–O bond formation. Indeed, if water activation on Sn is bypassed in this way, and the adsorbed CO reacts water molecule directly to form COOH, then the energy increase is reduced by 0.3 eV.

The other elementary steps of CO electro-oxidation on Pt₃Sn are basically downhill in energy. We calculated the energy barrier of CO and OH combination after the OH is kinetically formed on Sn. The energy barrier is only 0.2 eV, as shown in Figure 5b, due to the weak adsorption of CO on Pt and OH on Sn, respectively.

The calculated PES of CO electro-oxidation on Pt₃Mo and Pt₃Ru surfaces, assuming the same reaction mechanism, are also shown in Figure 5a. Ru and Mo both destabilize CO adsorption on adjacent Pt by 0.2 eV. Water activation on Ru and Mo sites are easier as compared to on Sn. On a Ru site, the water activation requires an energy input of 0.5 eV, while the step is spontaneous on the Mo site at $U = 0$ V. It should be noted that the Eley-Rideal mechanism is not viable on Pt₃Ru because the Ru site is covered with CO before water can be activated on the site. Consequently, the CO adlayer is so dense that water molecules cannot get to the surface to react with adsorbed CO. For the Pt₃Mo(111) surface,

water activation is no longer the rate-determining step. Instead, the reaction of CO and OH is endothermic by 0.5 eV and the energy barrier of the step is calculated to be 0.6 eV, as shown in Figure 5b.

Computational screening of Pt₃M CO-tolerant electrocatalysts

Pt₃M catalysts are screened by evaluating their surface phase diagrams. The dopants M include d-block and p-block metals in the 4th, 5th, and 6th rows of the periodic table. The surface phase diagrams are shown in Figure 6. With the comprehensive understanding of the surface states of Pt, Pt₃Sn, Pt₃Ru, and Pt₃Mo developed above, we target our search for other Pt₃Mo-like and Pt₃Sn-like surface phase diagrams. It can be seen that Pt₃Sc, Pt₃Ti, Pt₃V, Pt₃Y, Pt₃Zr, Pt₃Nb, Pt₃Hf, Pt₃Ta, Pt₃W, and Pt₃Re have Pt₃Mo-like surface phase diagrams, in which CO and oxygenated species can be co-adsorbed at low applied potentials (0.2 – 0.4 V) and CO coverage is 0.5 ML or 0.25 ML at $p_{\text{CO}} = 10^{-5}$ atm. Pt₃Ge, Pt₃In, Pt₃Hg, Pt₃Tl, Pt₃Pb, and Pt₃Bi are Pt₃Sn-like alloys in that they can effectively reduce the CO coverage to 0.25 ML at $p_{\text{CO}} = 10^{-5}$ atm.

In the above study, we did not consider the stability of these alloys. The identified candidates based on activity descriptors can be subject to further screening based on their alloying/segregation tendencies. The DFT-calculated formation energies and the surface segregation energies for various Pt-based alloys can be found in Ref. 30 and 31, respectively. These data can serve as guideline for experimentalists to narrow down candidates for synthesis.

Conclusion

In this work, we employed first-principles thermodynamics to develop an comprehensive understanding of the surface states of Pt and Pt alloy surfaces under reaction conditions of the CO electro-oxidation reaction and the HOR. We find that CO electro-oxidation on Pt₃Mo

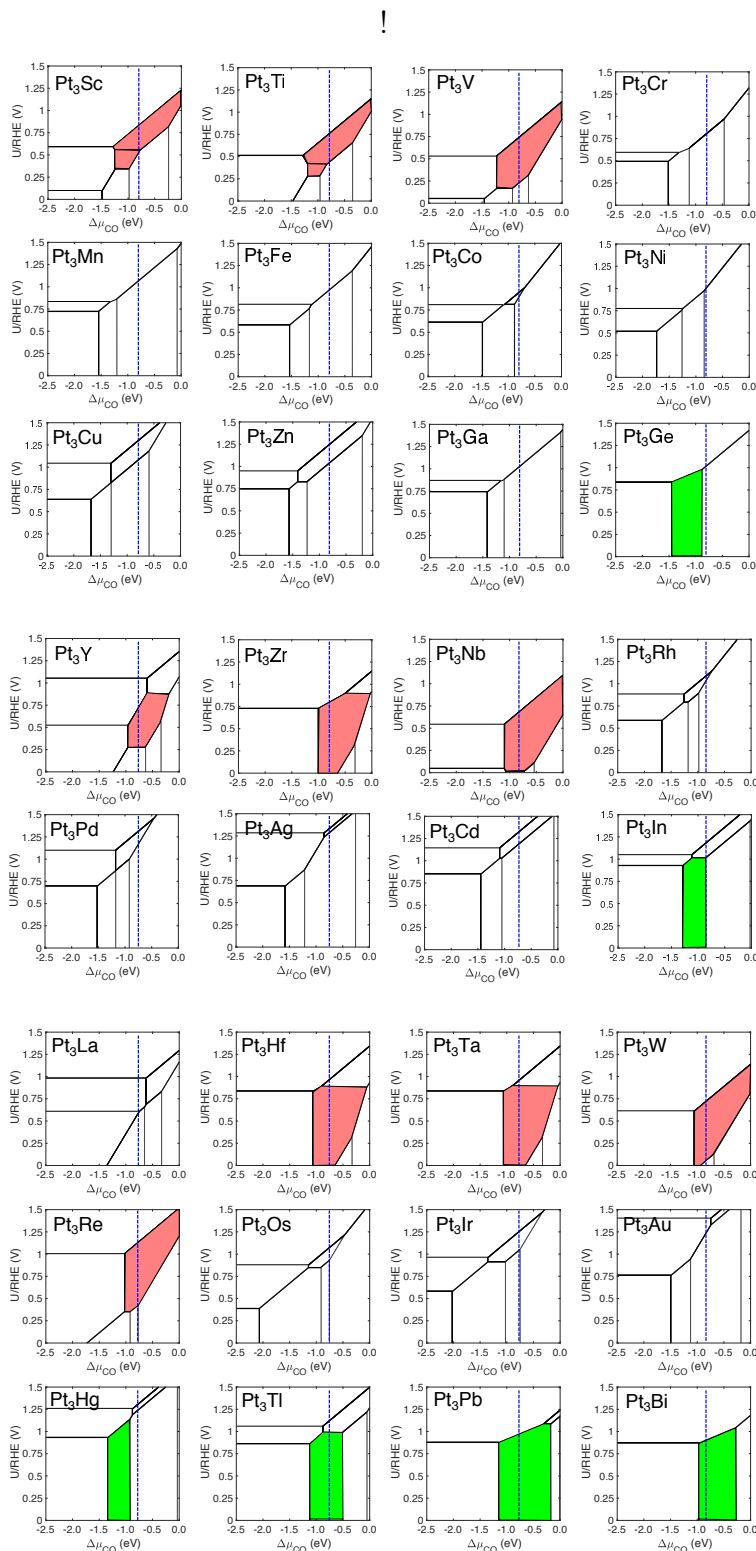


Figure 6: Surface phase diagrams for $\text{Pt}_3\text{M}(111)$ for various alloying metals, M. The blue dashed line indicates the chemical potential of CO gas corresponding to a partial pressure of 10^{-5} atm. The pink patches indicate CO/O mixed phases present at low potentials, 0.1 V – 0.4 V. The green patches indicate a 0.25 ML CO coverage phase.

follows a true bifunctional mechanism, in which Mo serves exclusively for water oxidation. Ru cannot activate water on its own, so the electro-oxidation on Pt₃Ru follows a pseudo-bifunctional mechanism. In contrast, CO electro-oxidation on Pt₃Sn follows an Eley-Rideal mechanism since Sn cannot effectively oxidize water at the experimentally observed onset potential. The negative reaction order of CO electro-oxidation as a function of CO partial pressure on Pt₃Mo and Pt₃Ru is due to the competitive adsorption of CO and oxygenated species on Mo and Ru dopants. Comparatively, CO does not adsorb on the Sn sites, so increasing the CO partial pressure increases the CO coverage on Pt sites leading to the observed positive reaction order. Regarding the HOR in the presence of CO, the oxidative CO removal on Pt₃Mo and Pt₃Sn contributes to the CO tolerance by reducing the steady-state CO coverage at low potential. The onset potential of CO electro-oxidation on Pt₃Ru is not low enough to facilitate the removal of CO at the low potential of the HOR.

The ligand effects of Ru, Mo, and Sn dopants make CO adsorption on Pt sites weaker in all three cases. Sn dramatically destabilizes CO adsorption on Pt by 0.5 eV at the atop site, which leads to a significant reduction in the CO coverage. Mo and Ru only mildly destabilize CO adsorption atop Pt by 0.2 and 0.1 eV, respectively.

In summary, we attribute the CO-tolerance on Pt₃Mo and Pt₃Sn to oxidative CO removal and destabilized CO adsorption on Pt. For Pt₃Ru, the CO destabilizing effect is the major reason for the CO-tolerance. Based on this understanding, we used first-principles thermodynamics as a screening tool to search for Pt₃M electrocatalysts with Pt₃Mo- and Pt₃Sn-like surface phase diagrams. A number of promising candidates are proposed.

Acknowledgement

This work is supported by the Department of Energy under contract DE-SC0010576 and the Welch Foundation under grant F-1841. The calculations were done at the National Energy Research Scientific Computing Center and the Texas Advanced Computing Center. Yulu

Liu thanks the China Scholarship Council for financial support. The authors thank Hao Li and Wanglai Cen for valuable discussions.

References

- (1) Gasteiger, H. A.; Marković, N.; Ross, P. N.; Cairns, E. J. Carbon monoxide electrooxidation on well-characterized platinum-ruthenium alloys. *J. Phys. Chem.* **1994**, *98*, 617–625.
- (2) Gasteiger, H. A.; Marković, N. M.; Ross, P. N. H₂ and CO electrooxidation on well-characterized Pt, Ru, and Pt-Ru. 1. Rotating disk electrode studies of the pure gases including temperature effects. *J. Phys. Chem.* **1995**, *99*, 8290–8301.
- (3) Gasteiger, H. A.; Marković, N. M.; Ross, P. N. H₂ and CO Electrooxidation on Well-Characterized Pt, Ru, and Pt-Ru. 2. Rotating Disk Electrode Studies of CO/H₂ Mixtures at 62° C. *J. Phys. Chem.* **1995**, *99*, 16757–16767.
- (4) Jusys, Z.; Kaiser, J.; Behm, R. Composition and activity of high surface area PtRu catalysts towards adsorbed CO and methanol electrooxidation: A DEMS study. *Electrochim. Acta* **2002**, *47*, 3693–3706.
- (5) Paulus, U.; Endruschat, U.; Feldmeyer, G.; Schmidt, T.; Bönnemann, H.; Behm, R. New PtRu Alloy Colloids as Precursors for Fuel Cell Catalysts. *J. Catal.* **2000**, *195*, 383–393.
- (6) Grgur, B. N.; Zhuang, G.; Marković, N. M.; Ross, P. N. Electrooxidation of H₂/CO Mixtures on a Well-Characterized Pt₇₅Mo₂₅ Alloy Surface. *J. Phys. Chem. B* **1997**, *101*, 3910–3913.
- (7) Grgur, B. N.; Marković, N. M.; Ross, P. N. Electrooxidation of H₂, CO, and H₂/CO

- Mixtures on a Well-Characterized Pt₇₀Mo₃₀ Bulk Alloy Electrode. *J. Phys. Chem. B* **1998**, *102*, 2494–2501.
- (8) Mukerjee, S.; Urian, R. C.; Lee, S. J.; Ticianelli, E. A.; McBreen, J. Electrocatalysis of CO Tolerance by Carbon-Supported PtMo Electrocatalysts in PEMFCs. *J. Electrochem. Soc.* **2004**, *151*, A1094.
- (9) Marković, N. M.; Widelôv, A.; Ross, P. N.; Monteiro, O. R.; Brown, I. G. Electrooxidation of CO and CO/H₂ mixtures on a Pt-Sn catalyst prepared by an implantation method. *Catal. Lett.* **1997**, *43*, 161–166.
- (10) Stamenković, V. R.; Matthias, A.; Christopher, A. L.; Gallagher, M. E.; Ross, P. N.; Marković, N. M. Surface Chemistry on Bimetallic Alloy Surfaces: Adsorption of Anions and Oxidation of CO on Pt₃Sn(111). *J. Am. Chem. Soc.* **2003**, *125*, 2736–2745.
- (11) Stamenković, V.; Arenz, M.; Blizanac, B. B.; Mayrhofer, K. J. J.; Ross, P. N.; Marković, N. M. In situ CO oxidation on well characterized Pt₃Sn(hkl) surfaces: A selective review. *Surf. Sci.* **2005**, *576*, 145–157.
- (12) Gasteiger, H. A.; Marković, N. M.; Ross, P. N. Structural effects in electrocatalysis: electrooxidation of carbon monoxide on Pt₃Sn single-crystal alloy surfaces. *Catal. Lett.* **1996**, *36*, 1–8.
- (13) Liu, Y.; Li, D.; Stamenkovic, V. R.; Soled, S.; Henao, J. D.; Sun, S. Synthesis of Pt₃Sn alloy nanoparticles and their catalysis for electro-oxidation of CO and methanol. *ACS Catal.* **2011**, *1*, 1719–1723.
- (14) Marković, N. M.; Ross, P. N. Electrocatalysts by design: from the tailored surface to a commercial catalyst. *Electrochim. Acta* **2000**, *45*, 4101 – 4115.
- (15) Kresse, G.; Hafner, J. Ab initio molecular dynamics for liquid metals. *Phys. Rev. B* **1993**, *47*, 558.

- (16) Kresse, G.; Furthmüller, J. Efficiency of ab-initio total energy calculations for metals and semiconductors using a plane-wave basis set. *Comput. Mater. Sci.* **1996**, *6*, 15–50.
- (17) Kresse, G.; Furthmüller, J. Efficient iterative schemes for ab initio total-energy calculations using a plane-wave basis set. *Phys. Rev. B* **1996**, *54*, 11169.
- (18) Hammer, B.; Hansen, L. B.; Nørskov, J. K. Improved adsorption energetics within density-functional theory using revised Perdew-Burke-Ernzerhof functionals. *Phys. Rev. B* **1999**, *59*, 7413–7421.
- (19) Blöchl, P. E. Projector augmented-wave method. *Phys. Rev. B* **1994**, *50*, 17953.
- (20) Monkhorst, H. J.; Pack, J. D. Special points for Brillouin-zone integrations. *Phys. Rev. B* **1976**, *13*, 5188–5192.
- (21) Li, H.; Evans, E.; Mullins, C. B.; Henkelman, G. Ethanol Decomposition on Pd-Au Alloy Catalysts. *J. Phys. Chem. C* **2018**, *122*, 22024–22032.
- (22) Nørskov, J. K.; Rossmeisl, J.; Logadottir, A.; Lindqvist, L.; Kitchin, J. R.; Bligaard, T.; Jónsson, H. Origin of the overpotential for oxygen reduction at a fuel-cell cathode. *J. Phys. Chem. B* **2004**, *108*, 17886–17892.
- (23) Hansen, H. A.; Rossmeisl, J.; Nørskov, J. K. Surface Pourbaix diagrams and oxygen reduction activity of Pt, Ag and Ni(111) surfaces studied by DFT. *Phys. Chem. Chem. Phys.* **2008**, *10*, 3722.
- (24) Reuter, K.; Scheffler, M. Composition and structure of the RuO₂ surface in an O₂ and CO environment: Implications for the catalytic formation of CO₂. *Phys. Rev. B* **2003**, *68*, 045407.
- (25) Chase, M. W. J. *NIST-JANAF Thermochemical Tables, 4th Edition*; American Institute of Physics: New York, 1998.

- (26) Gholizadeh, R.; Yu, Y.-X. $\text{N}_2\text{O}+\text{CO}$ reaction over Si- and Se-doped graphenes: An ab initio DFT study. *Applied Surface Science* **2015**, *357*, 1187–1195.
- (27) Villegas, I.; Weaver, M. J. Carbon monoxide adlayer structures on platinum (111) electrodes: A synergy between in-situ scanning tunneling microscopy and infrared spectroscopy. *J. Chem. Phys.* **1994**, *101*, 1648–1660.
- (28) Marković, N. M.; Grgur, B. N.; Lucas, C. A.; Ross, P. N. Electrooxidation of CO and H_2/CO Mixtures on Pt(111) in Acid Solutions. *J. Phys. Chem. B* **1999**, *103*, 487–495.
- (29) Krasnikov, S. A.; Murphy, S.; Berdunov, N.; McCoy, A. P.; Radican, K.; Shvets, I. V. *Nanotechnology* **2010**, *21*, 335301.
- (30) Bligaard, T.; Andersson, M. P.; Jacobsen, K. W.; Skriver, H. L.; Christensen, C. H.; Nørskov, J. K. Electronic-Structure-Based Design of Ordered Alloys. *MRS Bulletin* **2006**, *31*, 986–990.
- (31) Ruban, A. V.; Skriver, H. L.; Nørskov, J. K. Surface segregation energies in transition-metal alloys. *Phys. Rev. B* **1999**, *59*, 15990–16000.